Biomedical Optics EXPRESS

# Simultaneous photoacoustic and optically mediated ultrasound microscopy: an *in vivo* study

**Pavel Subochev,[1,*] Anna Orlova,[1] Marina Shirmanova,[2,3] Anna Postnikova,[1] and Ilya Turchin[1]**

[1] *Institute of Applied Physics RAS, 46 Ulyanov Street, Nizhniy Novgorod, Russia*
[2] *Lobachevsky State University of Nizhny Novgorod, 19 Gagarin Avenue, Nizhniy Novgorod, Russia*
[3] *Nizhny Novgorod State Medical Academy, Nizhniy Novgorod, Russia*
[*] *Pavel.Subochev@gmail.com*

**Abstract:** We propose the use of thermoelastic (TE) excitation of an ultrasonic (US) detector by backscattered laser radiation as a means of upgrading a single-modality photoacoustic (PA) microscope to dual-modality PA/US imaging at minimal cost. The upgraded scanning head of our dual-modality microscope consists of a fiber bundle with 14 output arms and a 32MHz polyvinylidene difluoride (PVDF) detector with a 34 MHz bandwidth (−6 dB level), 12.7 mm focal length, and a 0.25 numerical aperture. A single optical pulse delivered through the fiber bundle to the biotissue being investigated, in combination with a metalized surface on the PVDF detector allows us to obtain both PA and US A-scans. To demonstrate the in vivo capabilities of the proposed method we present the results of bimodal imaging of the brain of a newborn rat, a mouse tail and a mouse tumor.



**OCIS codes:** (170.5120) Photoacoustic imaging; (170.7180) Ultrasound diagnostics.

## References and links

1. P. Beard, "Biomedical photoacoustic imaging," Interface Focus **1**(4), 602–631 (2011).
2. I. Y. Petrov, Y. Petrov, D. S. Prough, D. J. Deyo, I. Cicenaite, and R. O. Esenaliev, "Optoacoustic monitoring of cerebral venous blood oxygenation through extracerebral blood," Biomed. Opt. Express **3**(1), 125–136 (2012).
3. J. Jose, D. J. Grootendorst, T. W. Vijn, M. W. Wouters, H. Van Boven, T. G. Van Leeuwen, W. Steenbergen, T. J. Ruers, and S. Manohar, "Initial results of imaging melanoma metastasis in resected human lymph nodes using photoacoustic computed tomography," J. Biomed. Opt. **16**, 096021 (2011).
4. T. J. Allen, A. Hall, A. P. Dhillon, J. S. Owen, and P. C. Beard, "Spectroscopic photoacoustic imaging of lipid-rich plaques in the human aorta in the 740 to 1400 nm wavelength range," J. Biomed. Opt. **17**(6), 061209 (2012).
5. A. Taruttis, S. Morscher, N. C. Burton, D. Razansky, and V. Ntziachristos, "Fast multispectral optoacoustic tomography (MSOT) for dynamic imaging of pharmacokinetics and biodistribution in multiple organs," PLoS ONE **7**(1), e30491 (2012).
6. Y.-S. Chen, W. Frey, S. Kim, P. Kruizinga, K. Homan, and S. Emelianov, "Silica-coated gold nanorods as photoacoustic signal nanoamplifiers," Nano Lett. **11**(2), 348–354 (2011).
7. J. Laufer, A. Jathoul, M. Pule, and P. Beard, "In vitro characterization of genetically expressed absorbing proteins using photoacoustic spectroscopy," Biomed. Opt. Express **4**(11), 2477–2490 (2013).
8. J. Powers and F. Kremkau, "Medical ultrasound systems," Interface Focus **1**(4), 477–489 (2011).
9. A. A. Oraevsky, S. A. Ermilov, A. Conjusteau, P. Brecht, V. Nadvoretskiy, R. Su, D. G. Herzog, B. Clingman, and J. Zalev, "Dual modality imaging system for coregistered functional and anatomical mapping," (WO Patent 2,013,067,419, 2013).
10. R. Bouchard, O. Sahin, and S. Emelianov, "Ultrasound-guided photoacoustic imaging: current state and future development," IEEE Trans. Ultrason. Ferroelectr. Freq. Control **61**(3), 450–466 (2014).
11. J. J. Niederhauser, M. Jaeger, R. Lemor, P. Weber, and M. Frenz, "Combined ultrasound and optoacoustic system for real-time high-contrast vascular imaging in vivo," IEEE Trans. Med. Imaging **24**(4), 436–440 (2005).
12. A. Needles, A. Heinmiller, J. Sun, C. Theodoropoulos, D. Bates, D. Hirson, M. Yin, and F. S. Foster, "Development and initial application of a fully integrated photoacoustic micro-ultrasound system," IEEE Trans. Ultrason. Ferroelectr. Freq. Control **60**(5), 888–897 (2013).
13. K. Daoudi, P. J. van den Berg, O. Rabot, A. Kohl, S. Tisserand, P. Brands, and W. Steenbergen, "Handheld probe integrating laser diode and ultrasound transducer array for ultrasound/photoacoustic dual modality imaging," Opt. Express **22**(21), 26365–26374 (2014).

#226129 - $15.00 USD Received 31 Oct 2014; revised 9 Dec 2014; accepted 23 Dec 2014; published 29 Jan 2015

14. J. Gateau, A. Chekkoury, and V. Ntziachristos, "Ultra-wideband three-dimensional optoacoustic tomography," Opt. Lett. **38**(22), 4671–4674 (2013).
15. X. Wang, J. B. Fowlkes, J. M. Cannata, C. Hu, and P. L. Carson, "Photoacoustic imaging with a commercial ultrasound system and a custom probe," Ultrasound Med. Biol. **37**(3), 484–492 (2011).
16. V. G. Andreev, A. A. Karabutov, and A. A. Oraevsky, "Detection of ultrawide-band ultrasound pulses in optoacoustic tomography," IEEE Trans. Ultrason. Ferroelectr. Freq. Control **50**(10), 1383–1390 (2003).
17. V. Kozhushko, T. Khokhlova, A. Zharinov, I. Pelivanov, V. Solomatin, and A. Karabutov, "Focused array transducer for two-dimensional optoacoustic tomography," J. Acoust. Soc. Am. **116**(3), 1498–1506 (2004).
18. M. Jaeger, D. Harris-Birtill, A. Gertsch, E. O'Flynn, and J. Bamber, "Deformation-compensated averaging for clutter reduction in epiphotoacoustic imaging *in vivo*," J. Biomed. Opt. **17**(6), 066007 (2012).
19. P. Subochev, A. Katichev, A. Morozov, A. Orlova, V. Kamensky, and I. Turchin, "Simultaneous photoacoustic and optically mediated ultrasound microscopy: phantom study," Opt. Lett. **37**(22), 4606–4608 (2012).
20. J. Xia, C. Huang, K. Maslov, M. A. Anastasio, and L. V. Wang, "Enhancement of photoacoustic tomography by ultrasonic computed tomography based on optical excitation of elements of a full-ring transducer array," Opt. Lett. **38**(16), 3140–3143 (2013).
21. J. Jose, R. G. Willemink, W. Steenbergen, C. H. Slump, T. G. van Leeuwen, and S. Manohar, "Speed-of-sound compensated photoacoustic tomography for accurate imaging," Med. Phys. **39**(12), 7262–7271 (2012).
22. G. Wurzinger, R. Nuster, N. Schmitner, S. Gratt, D. Meyer, and G. Paltauf, "Simultaneous three-dimensional photoacoustic and laser-ultrasound tomography," Biomed. Opt. Express **4**(8), 1380–1389 (2013).
23. D. Tsyboulski, A. Conjusteau, and A. Oraevsky, "Dual modality optoacoustic and laser ultrasound endoscopy system," in *SPIE BiOS*, (International Society for Optics and Photonics, 2014), 89432S–89432S–89435.
24. T. F. Fehm, X. L. Deán-Ben, and D. Razansky, "Four dimensional hybrid ultrasound and optoacoustic imaging via passive element optical excitation in a hand-held probe," Appl. Phys. Lett. **105**(17), 173505 (2014).
25. H. W. Baac, J. G. Ok, A. Maxwell, K.-T. Lee, Y.-C. Chen, A. J. Hart, Z. Xu, E. Yoon, and L. J. Guo, "Carbon-nanotube optoacoustic lens for focused ultrasound generation and high-precision targeted therapy," Sci. Rep. **2**, 989 (2012).
26. X. Zou, N. Wu, Y. Tian, and X. Wang, "Broadband miniature fiber optic ultrasound generator," Opt. Express **22**(15), 18119–18127 (2014).
27. G. J. Diebold, T. Sun, and M. I. Khan, "Photoacoustic monopole radiation in one, two, and three dimensions," Phys. Rev. Lett. **67**(24), 3384–3387 (1991).
28. S. L. Jacques, "Optical properties of biological tissues: a review," Phys. Med. Biol. **58**(11), R37–R61 (2013).
29. Z. Xie, L. V. Wang, and H. F. Zhang, "Optical fluence distribution study in tissue in dark-field confocal photoacoustic microscopy using a modified Monte Carlo convolution method," Appl. Opt. **48**(17), 3204–3211 (2009).
30. H. F. Zhang, K. Maslov, G. Stoica, and L. V. Wang, "Functional photoacoustic microscopy for high-resolution and noninvasive in vivo imaging," Nat. Biotechnol. **24**(7), 848–851 (2006).
31. M. Omar, D. Soliman, J. Gateau, and V. Ntziachristos, "Ultrawideband reflection-mode optoacoustic mesoscopy," Opt. Lett. **39**(13), 3911–3914 (2014).
32. S. Kellnberger, N. C. Deliolanis, D. Queirós, G. Sergiadis, and V. Ntziachristos, "In vivo frequency domain optoacoustic tomography," Opt. Lett. **37**(16), 3423–3425 (2012).
33. B. Liu, R. Kruger, D. Reinecke, and K. M. Stantz, "Monitor hemoglobin concentration and oxygen saturation in living mouse tail using photoacoustic CT scanner," in *BiOS*, (International Society for Optics and Photonics, 2010), 756439.
34. *The Laboratory Mouse*, 2nd ed. Hans Hedrich ed. (Academic Press, 2012).
35. E. Guevara, R. Berti, I. Londono, N. Xie, P. Bellec, F. Lesage, and G. A. Lodygensky, "Imaging of an inflammatory injury in the newborn rat brain with photoacoustic tomography," PLoS ONE **8**(12), e83045 (2013).
36. J. Laufer, E. Zhang, G. Raivich, and P. Beard, "Three-dimensional noninvasive imaging of the vasculature in the mouse brain using a high resolution photoacoustic scanner," Appl. Opt. **48**(10), D299–D306 (2009).
37. E. Zhang, J. Laufer, and P. Beard, "Backward-mode multiwavelength photoacoustic scanner using a planar Fabry-Perot polymer film ultrasound sensor for high-resolution three-dimensional imaging of biological tissues," Appl. Opt. **47**(4), 561–577 (2008).
38. B. E. Treeby, E. Z. Zhang, and B. Cox, "Photoacoustic tomography in absorbing acoustic media using time reversal," Inverse Probl. **26**(11), 115003 (2010).
39. E. W. Stein, K. Maslov, and L. V. Wang, "Noninvasive, in vivo imaging of the mouse brain using photoacoustic microscopy," J. Appl. Phys. **105**(10), 102027 (2009).
40. V. Perekatova, I. Fiks, and P. Subochev, "Image Correction in Optoacoustic Microscopy. Numerical Simulation," Radiophys. Quantum Electron. **57**(1), 67–79 (2014).
41. M.-L. Li, H. E. Zhang, K. Maslov, G. Stoica, and L. V. Wang, "Improved in vivo photoacoustic microscopy based on a virtual-detector concept," Opt. Lett. **31**(4), 474–476 (2006).
42. Y. Jiang, A. Forbrich, T. Harrison, and R. J. Zemp, "Blood oxygen flux estimation with a combined photoacoustic and high-frequency ultrasound microscopy system: a phantom study," J. Biomed. Opt. **17**(3), 036012 (2012).
43. M. Jaeger, K. Gashi, H. G. Akarçay, G. Held, S. Peeters, T. Petrosyan, S. Preisser, M. Gruenig, and M. Frenz, "Real-time clinical clutter reduction in combined epi-optoacoustic and ultrasound imaging," Photonics & Lasers in Medicine (2014).
44. H. Won Baac, J. G. Ok, H. J. Park, T. Ling, S.-L. Chen, A. J. Hart, and L. J. Guo, "Carbon nanotube composite optoacoustic transmitters for strong and high frequency ultrasound generation," Appl. Phys. Lett. **97**(23), 234104 (2010).

#226129 - $15.00 USD Received 31 Oct 2014; revised 9 Dec 2014; accepted 23 Dec 2014; published 29 Jan 2015

45. M. Omar, J. Gateau, and V. Ntziachristos, "Raster-scan optoacoustic mesoscopy in the 25-125 MHz range," Opt. Lett. **38**(14), 2472–2474 (2013).
46. L. V. Wang, "Tutorial on photoacoustic microscopy and computed tomography," IEEE J. Sel. Top. Quantum Electron. **14**(1), 171–179 (2008).
47. Y. Zhou, W. Xing, K. I. Maslov, L. A. Cornelius, and L. V. Wang, "Handheld photoacoustic microscopy to detect melanoma depth in vivo," Opt. Lett. **39**(16), 4731–4734 (2014).

## 1. Introduction

Photoacoustic (PA) imaging is a modern method of biomedical visualization based on the detection of ultrasonic (US) pulses generated in the investigated medium as a result of the absorption of pulsed laser radiation by optical heterogeneities [1].

Hybrid PA methods combine the advantages of both diffuse optical and US tomographies. In particular, the minimal scattering of US in biotissues provides hybrid PA methods with sub-millimeter resolution at diagnostic depths of between several millimeters and several centimeters. Meanwhile, the optical absorption spectra of endogenous chromophores (hemoglobin [2], melanin [3], lipids [4], etc.) and exogenous markers (organic dyes [5], nanoparticles [6], fluorescent proteins [7], etc.) enable the corresponding PA imaging to have a level of contrast that is unachievable by the US methods alone [8].

In order to get complementary information about a variety of biotissue heterogeneities it is possible to combine PA imaging of the optical absorption of those tissues with the US imaging of their mechanical contrast [9, 10]. To upgrade a single-modality PA device to a dual-modality PA/US imaging system one needs to send probing US pulses into the tissue being investigated.

The PA devices used by many optoacoustic groups are based on commercial US transducers, which have an additional built-in functionality of generating probing US pulses through the use of electrical excitation. For example, the first successful implementation of real-time dual-modality US/PA tomography was reported by the Bernese optoacoustic group, using a 7.5 MHz commercial US array transducer [11]. The successful implementation of US/PA tomography with a 21 MHz commercial array transducer was subsequently reported in [12]. Based on recent developments in laser manufacturing technology, a diode stack laser has now been integrated inside a 7.5 MHz hand-held US array transducer to enable real-time dual-modality US/PA imaging within a portable US tomography system [13]. However, the more conventional US transducer arrays limit the frequency bandwidth of optoacoustic signals [14].

Possible cost-effective wideband alternatives to conventional US transducer arrays are custom-made PA probes [15] based on polyvinylidene difluoride (PVDF) polymer films. While, to ensure its PA imaging capabilities, the sensitive head of the PVDF detector array can be manufactured within the laboratory [16, 17], it can be more challenging to incorporate a means for the electrical excitation of the individual detector elements (to enable simultaneous PA/US imaging with the same probe). To overcome the challenges of electrical excitation of the PA detectors, the probing US pulses can alternatively be generated using thermoelastic excitation (TE) of the PA detector with pulsed laser radiation. The ability of laser generation of pulse-echo ultrasound by backscattered optical pulses was independently proposed in [18] for PA/US duplex tomography and in [19] for PA/US duplex microscopy. The idea of optical excitation of the probing US pulses was later implemented for PA/US tomography in paper [20]. However, instead of the simultaneous TE of the whole circular array by the backscattered laser radiation [18, 19], in paper [20] the TE of individual array elements was provided sequentially by direct laser irradiation.

To maximize the lateral resolution of the US modality with the spherically focused PA detector [19] it is important to provide TE of the curved surface of the focused detector. However, in the case of an unfocused PA detector it is common to provide TE of the external optically absorbing targets [21–24]. TE of novel optically absorbing materials enables pressures of over 50 MPa to be achieved at the focus of a high-intensity focused ultrasound generator [25] and a 0.64MPa pressure output from a fiber-optic ultrasound generator [26].

#226129 - $15.00 USD Received 31 Oct 2014; revised 9 Dec 2014; accepted 23 Dec 2014; published 29 Jan 2015

We have now upgraded the original PA/US microscope [19] by using laser excitation to generate the probing US pulses in a single-element PVDF detector, and, here, present its *in vivo* imaging capabilities.

## 2. Methods

The schematic of our upgraded experimental setup is presented in Fig. 1.

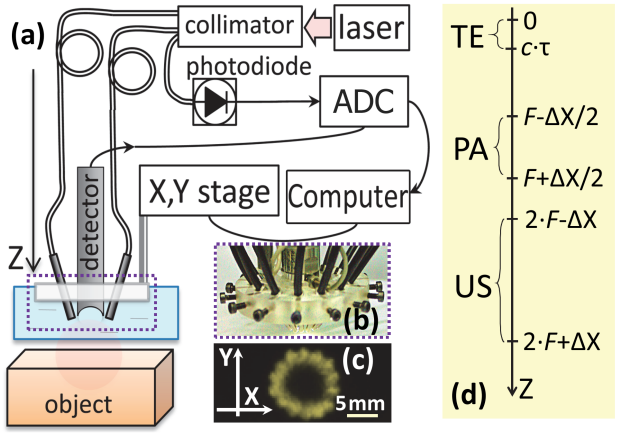


Fig. 1. The bimodal PA/US microscope which has been developed. (a) Schematic of the experimental setup. (b) Photograph of the upgraded scanning head. (c) Photograph of the optical fluence distribution on the surface of a piece of 80 g/m$^2$ paper in air. (d) Sketch of the information contained in an A-scan indicating the sequence of TE, PA, and US signals.

A tunable solid-state laser (LT-2214-PC) pumped by a 355 nm Q-switched laser (LS-2137/3) - both manufactured by "LOTIS TII", Belorussia, was used as the source of laser pulses. The average pulse duration of the laser system was 18 ns and this limited the axial spatial resolution to 28 μm [27] (taking into account that $c$ = 1.54 μm/ns is the average speed of sound in soft biological tissues). The ability to create laser pulses at any optical wavelength in the 410-690 nm and 700-2100 nm ranges allowed us to generate PA pulses in various tissue chromophores. However, for this *in vivo* study we have used only a 584 nm laser wavelength, corresponding to the isosbestic point of oxy- and deoxyhemoglobin [28].

To deliver the laser radiation to the object under investigation the output beam of the OPO laser was collimated with the fiber bundle. Instead of the custom-made fiber bundle used in [19] which had 8 output arms each of 2.5 mm diameter and 0.38 numerical aperture in water, we used a commercially available fiber bundle (Ceram Optec, Germany) with 16 arms each of 2.5 mm diameter as above and 0.17 numerical aperture in water. The first output arm of the fiber bundle was directed to a photodetector (DET10A, Thorlabs, USA) to eliminate the jitter effect of the laser. The second output arm was directed to a pyro sensor (ES11C, Thorlabs, USA) to measure the energy of each laser pulse. The other 14 output arms were each mounted at 40 degrees [29] to the axis of the PVDF detector and were directed at its focus (Fig. 1(b)). The 50% more numerous output arms, each with a 45% smaller NA, enabled the provision of an almost ring-shaped illumination pattern at the surface of the object under investigation [30] (Fig. 1(c)). According to the results [29] the larger inner radius of the ring-shaped illumination pattern provides higher PA imaging contrast. The maximum energy per pulse at the output of each fiber bundle was around 0.5 mJ at a pulse repetition rate of 10 Hz. The incident optical fluence was kept within 7.5 mJ/cm$^2$ to satisfy the standards of laser safety (20 mJ/cm$^2$).

Instead of the custom-made PVDF detector [19] with a central frequency of 35 MHz a bandwidth of 24 MHz (–6 dB level), a numerical aperture of 0.28 and a focal length of 9 mm, we used a commercially available PVDF detector, the PI-35-2 (Olympus-NDT, USA). While the numerical aperture and central frequency of the new detector were approximately the

#226129 - $15.00 USD Received 31 Oct 2014; revised 9 Dec 2014; accepted 23 Dec 2014; published 29 Jan 2015

same (NA = 0.25, f = 32 MHz), it had a 42% wider frequency band (Δf = 34 MHz) to improve the spectral capabilities of the PA modality of the microscope [31] and a 41% greater focal length (F = 12.7 mm) to ensure the detection of both PA and optically-mediated US A-scans at up to 6.4 mm depth without overlay [19]. The analog signals from the detector were sent through a custom-made AD8099-based low-noise amplifier and custom-made high-pass filter with a 1 MHz cut-off frequency to an Analog-to-Digital Converter (ADC) based on an NI5761 14-bit 250-MS/s Adapter Module with a NI FlexRIO FPGA Module PXI −7952R. The digitized signals were subjected to a Hilbert's transform.

The scanning head was mounted on two linear positioning slides with a maximum travel range of 6.25 mm (Automation Gages, USA) driven by AM-23-239-3 step motors (Advance Microsystems, USA) inside an immersion chamber filled with distilled water (Fig. 1(a)). Polyethylene film of thickness 60 μm covered the bottom of the immersion chamber to ensure the stationary contact of the object under investigation with the immersion chamber. The automation algorithm ensured sequential movement of the scanning head along the horizontal axes X and Y with a 10 Hz repetition rate of the laser pulses.

In order to provide 2D dual-modality visualization of the most informative square region (near the opto-acoustic focus of the microscope) the automation algorithm inquiries the definition of the scanning range $\Delta X$, the scanning step size $\delta x$, the focal length $F$, the average speed of sound $c$, and the average duration of the laser pulse $\tau$. Figure 1(d) schematically presents the sequence of signals to be registered by the PVDF detector at each of the $\Delta X/\delta x$ scanning positions of the opto-acoustic head. The TE signal is detected during the time period from $t = 0$ (corresponds to the trigger signal from the photodetector) to $t = \tau$. The PA A-scan is being detected during the time period from $t = (F\text{-}\Delta X/2)/c$ to $t = (F + \Delta X/2)/c$, and this is then normalized in relation to the pulse laser energy. The US A-scan is detected during the time period from $t = (2\cdot F\text{-}\Delta X)/c$ to $t = (2\cdot F + \Delta X)/c$, and this is then normalized in relation to the maximum of the TE signal. To provide a better leveling of the PA and US signals at different tissue depths the PA A-scans $PA(Z)$ were multiplied by $\exp(-\gamma\cdot(Z\text{-}Z_0))$ and the US A-scans $US(Z)$ were multiplied by $\exp(-2\cdot\gamma\cdot(Z\text{-}Z_0))$, with $Z_0$ corresponding to the coordinate of the tissue surface and with $\gamma$ corresponding to the effective ultrasonic attenuation of the tissue. The maximum lateral PA/US resolution of the upgraded microscope was achieved at the focal depth, without using any beam-forming algorithms to improve its lateral resolution above or below the focus. The US lateral resolution is better than the PA lateral resolution, since both TE and PA detection are provided by the same aperture. The US axial resolution is better than the PA axial resolution, since the pulse-echo propagation of US pulses doubles the effective discretization frequency.

In order to estimate the imaging capabilities of the earlier PA/US microscope [19] we measured the lateral and axial size of 65 μm copper wire at ½ level of its PA/US image. Using the PA image we obtained a 200/70 μm lateral/axial size and using a US image we obtained 140/45 μm as the lateral/axial size. Taking into account the finite 65 μm diameter of the copper wire, the maximum lateral resolution for the PA/US modality of the previous microscope can be estimated as 135/75 μm, while its the PA/US modality axial resolution can be estimated as 70/45 μm. After performing similar phantom experiments with the upgraded PA/US microscope we estimated the maximum lateral resolution for the PA/US modality of the upgraded microscope as 130/80 μm and the axial resolution of its PA/US modality as 55/30 μm. With these improved imaging capabilities we proceeded with the bimodal *in vivo* visualization of small laboratory animals.

All animal subjects used for PA/US imaging were handled in accordance with the guidelines approved by the Ethical Committee of the Nizhny Novgorod State Medical Academy. A three day old outbred rat and an eight week old Balb/c mouse were used in the experiments. Before the investigation the rat was anaesthetized with an intraperitoneal injection of 50 mg/kg of Zoletil 100 and immobilized in a prone position. The mouse was anaesthetized with an intramuscular injection of Zoletil 100 (40 mg/kg) and with Rometar (10 mg/kg). To obtain images of the tail vessels, the mouse was fixed in the supine position, while a lateral position was used to obtain images of the internal structure of the mouse. To induce a

#226129 - $15.00 USD Received 31 Oct 2014; revised 9 Dec 2014; accepted 23 Dec 2014; published 29 Jan 2015

subcutaneous tumor $5x10^5$ of Colo26 cells (murine colorectal carcinoma) suspended in 0.1 mL PBS were injected into the hind flank of the mouse. The experiments began on day 12 after tumor inoculation, when the tumor had a size of 12x7 mm.

### 3. Results and discussion

Figure 2(b) presents the results of the dual-modality 2D imaging of the mouse tail. In contrast to [32, 33], when the mouse tail imaging used single-modality PA imaging setups, the additional US modality of our bimodal microscope provides additional important structural information, such as the contours of the surface of the tail and the position of the spinal cord.

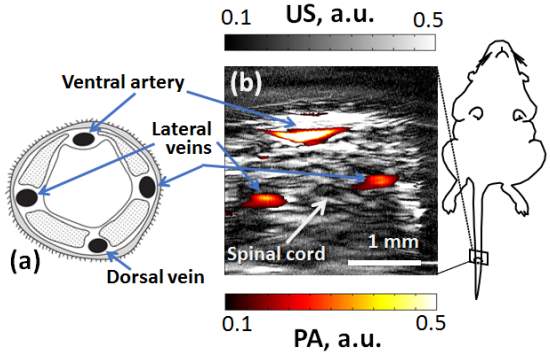


Fig. 2. The results of 2D bimodal PA/US visualization of a mouse tail *in vivo,* acquired with $\delta x$ = 4 μm steps of the scanning head. (a) Schematic of the major blood vessels inside the mouse tail according to [34]. (b) Overlay of the PA and US B-scans.

Although the intrinsic PA contrast should have also enabled identification of the dorsal vein (Fig. 2(a)), with the PA modality of our microscope we were only able to visualize three of the major blood vessels (Fig. 2(b)). The difficulties of PA visualization of the dorsal vein in the case of using limited-view scanning geometry have also been discussed in [33]. While the optoacoustic head of the [32] PA setup was rotated around the mouse's tail, the scanning optoacoustic head of our dual-modality PA/US microscope moved only along the horizontal X axis. Therefore, during the scanning procedure the bones within the tail blocked the PA pulses from being transmitted from the dorsal vein to the detector. Another factor that could have significantly reduce the PA signal from the dorsal vein is the non-homogeneous distribution of the optical fluence. The mutual geometry of the tail and the optical illumination make the dorsal vein the most shadowed blood vessel among the four (Fig. 2(a)).

Figure 3 presents the *in vivo* dual-modality images of the head of the infant rat. Since the wavelength of 584 nm corresponds to equal optical absorption by both oxygenated and deoxygenated forms of hemoglobin, the PA images reflect the total hemoglobin distribution. Therefore, the large dural venous sinuses can be located in the PA images. It is also possible to localize other zones characterized by their different volumes of blood. The anatomical context of these blood structures under the skull of the animal can be represented using the US image.

#226129 - $15.00 USD Received 31 Oct 2014; revised 9 Dec 2014; accepted 23 Dec 2014; published 29 Jan 2015

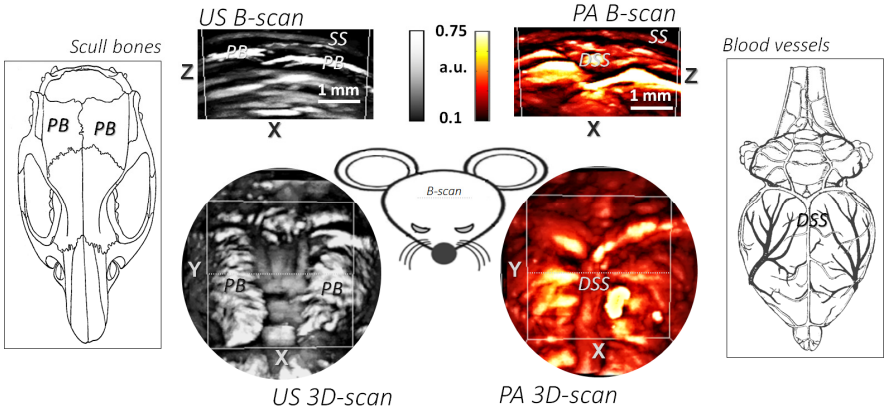


Fig. 3. Results of 3D bimodal PA/US visualization of newborn rat's head *in vivo* acquired with $\delta x = \delta y = 30$ µm steps of the scanning head. PB – parietal bones, SS – skin surface, DSS – dorsal sagittal sinus.

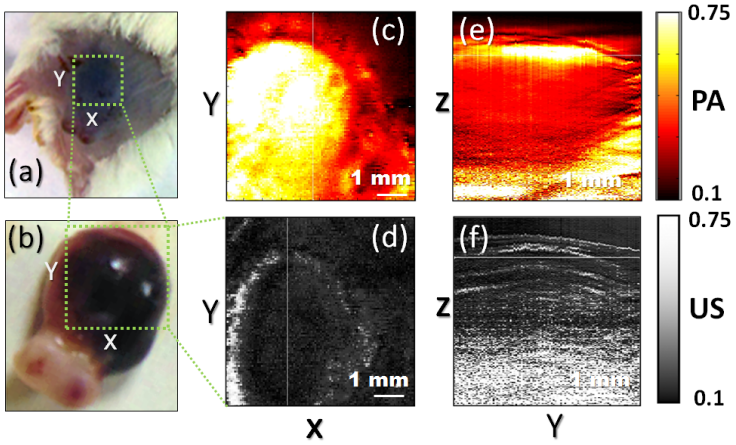


Fig. 4. Results of 3D bimodal PA/US visualization of a mouse tumor *in vivo* acquired with $\delta x = \delta y = 30$ µm steps of the scanning head. (a) Photograph of Colo26 tumor *in vivo* where the green square indicates the scanning range. (b) Photograph of dissected Colo26 tumor where the green square indicates the scanning range. (c) PA C-scan of the tumor. (d) US C-scan of the tumor. (e) PA B-scan of the tumor. (f) US B-scan of the tumor.

Dual-modality imaging of the brain of a 3-day old rat was also realized in paper [35] using a commercial PA/US tomography system (Vevo LAZR; Visualsonics, Canada), although the paper [35] was majorly focused on the imaging of inflammatory injury and the results, as presented, lack the 3D PA/US images that could have been compared with our own results (Fig. 3). In paper [36] a similar laser wavelength (590 nm) and a similar incident optical fluence (6.8 mJ/cm$^2$) were used to provide *ex vivo* single-modality PA imaging of mouse brain vasculature using a unique optical ultrasound imaging sensor [37] and reconstruction algorithm [38]. In paper [39] the *in vivo* images of the mouse brain vasculature were obtained at a 570 nm laser wavelength (at 12 m*J*/cm$^2$ incident fluence) using an acoustic-resolution PA microscope based on a 20MHz detector with a 0.64 numerical aperture. When compared with [39], due to the lower NA of our detector, the 3D images of the cortical vasculature obtained by the PA modality of our microscope lack the lateral spatial resolution (130 µm against 70 µm). On the other hand, the lower NA of our PA detector is a necessary trade-off for the ability to co-register the US signals with the PA signals without overlay (due to the delay line provided by the transparent skin-detector cavity [19]). When compared with [36], our PA images contain two types of artefacts. Those artefacts, caused by the limited depth of focus of

#226129 - $15.00 USD Received 31 Oct 2014; revised 9 Dec 2014; accepted 23 Dec 2014; published 29 Jan 2015

the detector, could be reduced by means of reconstruction algorithms [40, 41], while the motion artefacts, caused by the cardiac and respiratory activity of the anesthetized animal *in vivo* could be reduced by using a faster imaging system.

In Fig. 4 the results of the *in vivo* dual-modality PA/US imaging of an experimental subcutaneous Colo26 tumor are presented. The PA C-scan (Fig. 4(c)) represents an XY slice of the tumor at 1 mm depth from the skin surface. The tumor is seen as a region with high optical absorption, the optically absorbing heterogeneities are homogeneously distributed inside the top part of the tumor nodule. The increased but fairly uniform hemoglobin content of the subsurface tumor area may be associated with the high density of blood vessels or with local hemorrhaging (Fig. 4(b)). The B-scan of the tumor (Fig. 4(e)) enables the correct estimation of 4 mm as the maximum tumor depth. The center of the tumor is seen as an area with a low intensity PA signal as compared to the tumor surface (Fig. 4(e)), which could be connected with a low hemoglobin concentration in the central part of the tumor. However, since the intensity of the PA signal is proportional to both the local optical absorption and the fluence, the low PA contrast of the central region of the tumor could alternatively be caused by the shadow effect of the region with a high blood content.

With the US modality of the microscope we visualized the acoustic contrasts of the tumor. At 1 mm depth from the skin surface (Fig. 4(d)) the borders of the tumor can be seen. Unfortunately, the US B-scan (Fig. 4(f)) did not provide sufficient contrast for the lower tumor boundary to confirm the 4 mm thickness that was measured on the excised tumor (Fig. 4(b)). The low efficiency of the US imaging modality could be caused by the extensive hemorrhaging, since the resulting presence of a large quantity of an optical absorber could reduce the number of scattered photons needed for the TE generation of the probing US pulses.

## 4. Conclusion

Using small laboratory animals we evaluated the *in vivo* capabilities of our upgraded dual-modality PA/US imaging setup [19]. While the conventional approach to convert a single modality PA microscope to be applicable for dual-modality PA/US imaging is through the use of a pulser/receiver circuit [42], we have proposed a more cost-effective approach. Instead of the electrical generation of probing US pulses, the US imaging modality of our experimental setup is based on the «clutter» PA signal [43] generated due to the absorption of backscattered laser radiation by the metallized surface of the PA detector. The optical generation of probing US pulses can also be implemented as a result of external point [21] or planar [22] targets with strong optical absorbtion, such as carbon nanotube composites [44]. Although such external optically absorbing targets would provide additional bulk and affect the optimal resolution of the US modality of our dual-modality microscope, a thin layer of carbon nanotube composite [44] coated onto the surface of the PVDF detector would increase the efficiency of TE generation. Instead of relying on the diffuse photons scattered from the sample, TE of the detector can also be realized by directing one of the laser fibers at the detector. Possible other important upgrades of the existing dual-modality PA/US microscope would be the use of a compact laser with a higher pulse repetition rate [45] (with a temporal intensity average satisfying necessary safety limits [46]), along with a hand-held design of the scanning system [47]. A 2kHz pulse repetition rate would ensure faster PA/US dual-modality imaging with a 200-fold increase of the A-scan acquisition rate, while the hand-held design of the dual-modality PA/US microscope would ensure more verstile access to the *in vivo* objects. With these suggested upgrades it will be possible to study the clinical applicability of simultaneous PA/US bioimaging of the function and structure for human subjects.

## Acknowledgment

This work was supported financially by the Russian Science Foundation (project No14-15-00709). The authors are grateful to Roman Belyaev, Vladimir Vorobyev, and Sergey Pozhidaev for their engineering contributions to this work and to Dr. Alexander M. Reyman for his useful discussions.

#226129 - $15.00 USD Received 31 Oct 2014; revised 9 Dec 2014; accepted 23 Dec 2014; published 29 Jan 2015